Research Article Vol. 8, No. 7 / July 2021 / Optica 1013

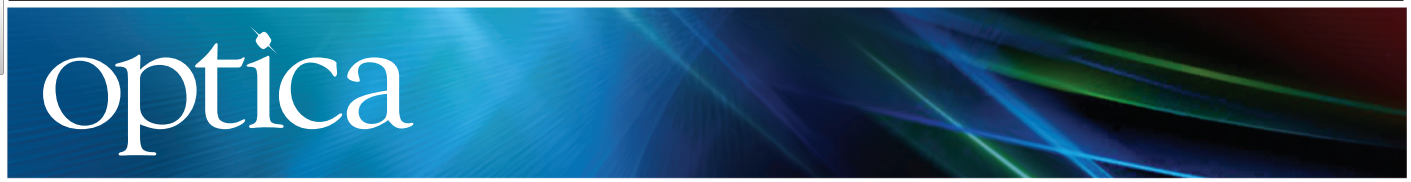

Modulating the polarization of broadband terahertz pulses from a spintronic emitter at rates up to 10 kHz

Oliver Gueckstock,[1,2] Lukáš Nádvorník,[1,2,3] Tom S. Seifert,[1,2] Martin Borchert,[1,2] Gerhard Jakob,[4] Georg Schmidt,[5] Georg Woltersdorf,[5] Mathias Kläui,[4] Martin Wolf,[2] and Tobias Kampfrath[1,2,*]

[1]Department of Physics, Freie Universität Berlin, 14195 Berlin, Germany
[2]Department of Physical Chemistry, Fritz Haber Institute of the Max Planck Society, 14195 Berlin, Germany
[3]Faculty of Mathematics and Physics, Charles University, 12116 Prague, Czech Republic
[4]Institut für Physik, Johannes-Gutenberg-Universität Mainz, 55128 Mainz, Germany
[5]Institut für Physik, Martin-Luther-Universität Halle-Wittenberg, 06120 Halle, Germany
*Corresponding author: tobias.kampfrath@fu-berlin.de

Received 3 May 2021; revised 13 June 2021; accepted 14 June 2021 (Doc. ID 430504); published 16 July 2021

Reliable modulation of terahertz electromagnetic waveforms is important for many applications. Here, we rapidly modulate the direction of the electric field of linearly polarized terahertz electromagnetic pulses with 1–30 THz bandwidth by applying time-dependent magnetic fields to a spintronic terahertz emitter. Polarity modulation of the terahertz field with more than 99% contrast at a rate of 10 kHz is achieved using a harmonic magnetic field. By adding a static magnetic field, we modulate the direction of the terahertz field between angles of, for instance, −53° and 53° at kilohertz rates. We believe our approach makes spintronic terahertz emitters a promising source for low-noise modulation spectroscopy and polarization-sensitive techniques such as ellipsometry at 1–30 THz.

https://doi.org/10.1364/OPTICA.430504

1. INTRODUCTION

Terahertz (THz) radiation is resonant with many low-energy modes in solid-state systems, gases, and liquids. Thus, THz spectroscopy allows one to characterize materials by their spectral fingerprint in the THz range. Tabletop sources of broadband THz radiation typically rely on difference-frequency mixing of femtosecond laser pulses in suitable media [1], resulting in sub-picosecond THz electromagnetic transients.

Modulation of the polarity (±) and, more generally, direction of the peak field of linearly polarized THz pulses is highly desirable for all kinds of modulation spectroscopy [2,3]. Examples include lock-in-type low-noise detection, linear spectroscopy of anisotropic samples, and the separation of symmetric and antisymmetric responses with respect to the driving THz field in nonlinear spectroscopy. However, rapid modulation of the polarity and direction of the polarization of broadband THz pulses remains challenging [4].

Amplitude modulation can easily be achieved by mechanical chopping of the THz beam or of the generating femtosecond laser beam. However, this approach only allows one to modulate (multiply) the global amplitude of the THz pulse with 0 and 1. Modulation of neither the polarity nor the direction of the THz field is possible, and half of the THz power is lost. The polarization modulation of a THz beam was achieved by rotating a THz retardation plate [5,6]. As the plate is rotated mechanically, a modulation frequency above 100 Hz is difficult to reach, and the THz bandwidth is limited by the retardation plate. Shaping of the THz pulse polarization is also possible with a combination of a THz grating [7] and a spatial light modulator [8]. However, such optical setup is costly and requires very precise adjustment.

Polarity modulation (PM) and direction modulation (DM) of the peak field of linearly polarized THz pulses is also possible through direct modulation of the THz generation process. In photoconductive antennas, PM was implemented by modulating the bias voltage [9–11]. DM is more challenging because it requires dual photoconductive antennas with identical responses to realize a clean modulation between angles $\pm\theta_0$ [11]. For optical rectification in suitable transparent nonlinear optical crystals [8,12], the polarization of the emitted THz pulse can be controlled by the polarization of the pump beam. DM, thus, requires a costly optical modulator and special nonlinear optical materials [13].

Spintronic THz emitters (STEs), a recently developed THz-emitter class [14–22], offer interesting opportunities for PM and DM. As schematically shown in Fig. 1(a), an STE typically consists of a ferromagnetic layer (F) with magnetization $\boldsymbol{M}$ and one [23–25] or two [14] adjacent nonmagnetic layers (N). A femtosecond laser pulse is incident on the STE and launches a spin current with density j_s from the F to N [26]. Through the inverse spin Hall

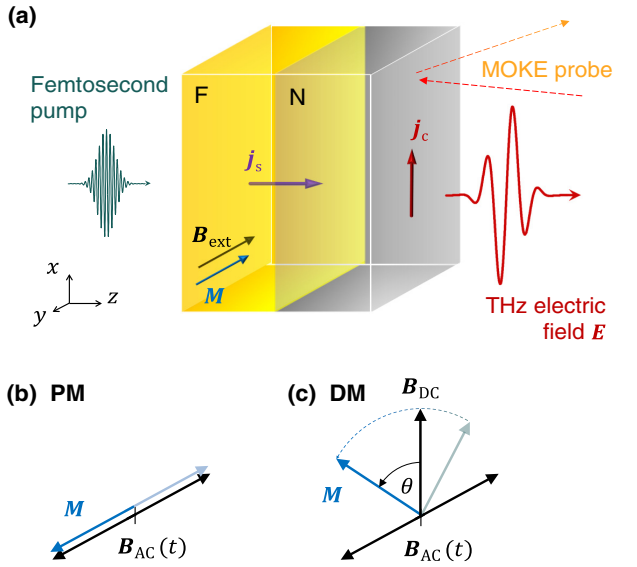

Fig. 1. Polarization modulation of THz pulses. (a) In a spintronic THz emitter (STE), an incident femtosecond laser pulse drives spin transport from a ferromagnetic (F) into an adjacent nonmagnetic (N) layer. By the inverse spin Hall effect, the spin current j_s is converted into a transverse charge current j_c that emits THz radiation. The resulting THz field $\boldsymbol{E}$ is linearly polarized and perpendicular to the magnetization $\boldsymbol{M}$ of the F layer. We modulate the direction of $\boldsymbol{M}$ and, thus, $\boldsymbol{E}$ by an external in-plane magnetic field $\boldsymbol{B}_{ext}$. The direction of $\boldsymbol{M}$ is monitored by means of the magneto-optic Kerr effect (MOKE). (b) In polarity-modulation (PM) mode, $\boldsymbol{B}_{ext} = \boldsymbol{B}_{AC}$ is a harmonic AC field $\boldsymbol{B}_{AC}(t) = \boldsymbol{u}_y B_{AC}(t)$ with $B_{AC}(t) = B_{AC0}\cos(2\pi f_{AC} t)$ from an electromagnet, thereby alternating the $\boldsymbol{M}$ direction between $\pm\boldsymbol{u}_y$. (c) In the more general direction-modulation (DM) mode, $\boldsymbol{B}_{AC}(t)$ is superimposed by a perpendicular DC magnetic field $\boldsymbol{B}_{DC} = B_{DC}\boldsymbol{u}_x$ from a permanent magnet. The angle $\theta(t)$ of the resulting $\boldsymbol{B}_{ext} = \boldsymbol{B}_{AC} + \boldsymbol{B}_{DC}$ and, thus, $\boldsymbol{M}$ oscillates continuously between values $\pm\theta_0$.

effect (ISHE) of the N material, j_s is converted into a transverse charge current with density $j_c = \gamma j_s$, where γ is the spin-Hall angle [Fig. 1(a)]. As the driving laser pulse has femtosecond duration, j_c is time-dependent and acts like an electric dipole that emits an electromagnetic pulse with frequencies extending into the THz range.

STEs have very interesting features: (i) They cover a wide bandwidth, in particular the region from 5–15 THz [14]. (ii) They operate with a very broad range of pump wavelengths [27,28]. (iii) They can be upscaled along with the laser power to generate THz field strengths reaching 0.3 MV/cm [15,29]. (iv) Due to the underlying physics, the THz electric field $\boldsymbol{E}$ is linearly polarized and perpendicular to the STE magnetization vector $\boldsymbol{M}$, as shown in Fig. 1(a) [14]. Thus, modulating the direction of $\boldsymbol{M}$ allows one to modulate the THz polarization.

In this paper, we demonstrate PM and DM of the polarization of broadband THz pulses from an STE at frequencies up to 10 kHz by a time-dependent external magnetic field. We believe our results open up promising routes toward modulation spectroscopy with THz radiation.

2. EXPERIMENTAL DETAILS

Our STE is a commercially available metallic thin-film THz emitter on a transparent z-cut sapphire substrate (TeraSpinTec GmbH). In our THz emission setup, the STE is excited by a femtosecond laser pulse (center wavelength 800 nm, pulse energy 1 nJ, repetition rate 80 MHz) from a laser oscillator, as shown in Fig. 1(a). The induced THz electromagnetic pulse is linearly polarized, and its electric field $\boldsymbol{E}$ directly behind the STE is perpendicular to the instantaneous magnetization $\boldsymbol{M}$ of the ferromagnetic layer; that is, $\boldsymbol{E} \propto \boldsymbol{M} \times \boldsymbol{u}_z$, where $\boldsymbol{u}_z$ is the unit vector along the z axis, as shown in Fig. 1(a). To achieve PM, we switch the magnetization vector $\boldsymbol{M}$ between opposite directions $\pm\boldsymbol{u}_y$ [Fig. 1(b)]. For DM, $\boldsymbol{M}$ is continuously and periodically rotated between two directions given by angles $\pm\theta_0$ [Fig. 1(c)].

To reject the remaining pump beam, a Ge wafer is placed behind the STE [30]. We characterize the transient THz electric field by electro-optic detection in a ZnTe (110) crystal (thickness 1 mm) using a co-propagating femtosecond probe pulse (0.6 nJ, 10 fs) from the same laser. Due to interaction with the THz electric field, the initially linearly polarized probe pulse acquires an ellipticity that is measured by a quarter-wave plate, a polarizing beam splitter, and two balanced photodiodes [31,32]. The resulting voltage signals S_x and S_y are linearly proportional to the components E_x and E_y of the THz electric field $\boldsymbol{E} \propto \boldsymbol{M} \times \boldsymbol{u}_z$. The THz electric-field components and corresponding signals are, therefore, expected to scale according to

$$S_x \propto E_x \propto -M_y, \quad S_y \propto E_y \propto M_x. \tag{1}$$

The component E_x or E_y is selected for detection by placing a rotatable THz wire-grid polarizer behind the STE. The azimuthal angle of the detection crystal and the probe-pulse polarization are set such that the detection unit is equally sensitive to E_x and E_y. For the PM mode, the voltages S_x and S_y are measured directly by a data acquisition card. For the DM experiment, the THz signal is also amplitude-modulated by mechanically chopping of the optical pump beam at about 32 kHz and demodulated by a lock-in amplifier. All experiments are conducted under ambient conditions in air if not stated otherwise.

The STE magnetization $\boldsymbol{M}$ is controlled by a time-dependent external magnetic field $\boldsymbol{B}_{ext}(t)$. When the coercive field and the in-plane magnetic anisotropy field of the STE's ferromagnetic layer is significantly smaller than $|\boldsymbol{B}_{ext}(t)|$, the direction of the sample magnetization is expected to directly follow the direction of the external field according to

$$\boldsymbol{M} = M_{sat}\boldsymbol{B}^0_{ext}. \tag{2}$$

Here, M_{sat} is the saturation magnetization, and $\boldsymbol{B}^0_{ext} = \boldsymbol{B}_{ext}/|\boldsymbol{B}_{ext}|$ is the unit direction of $\boldsymbol{B}_{ext}$. For PM [Fig. 1(b)], we apply a sinusoidal AC external magnetic field $\boldsymbol{B}_{AC}(t) = \boldsymbol{u}_y B_{AC}(t)$ along the y axis with $B_{AC}(t) = B_{AC0}\cos(2\pi f_{AC} t)$, amplitude B_{AC0}, and frequency f_{AC}. As a result, $\boldsymbol{M}$ is switched between the two states $\pm M_{sat}\boldsymbol{u}_y$. For DM [Fig. 1(c)], we add a static magnetic field $\boldsymbol{B}_{DC} = B_{DC}\boldsymbol{u}_x$ that is perpendicular to $\boldsymbol{B}_{AC}$. The resulting total external magnetic field is $\boldsymbol{B}_{ext} = \boldsymbol{B}_{DC} + \boldsymbol{B}_{AC}$; thus, $\boldsymbol{M}$ rotates continuously between angles $\pm\theta_0$. The instantaneous angle of $\boldsymbol{B}_{ext}$ is given by

$$\tan\theta(t) = \frac{B_{AC}(t)}{B_{DC}} = \frac{B_{AC0}}{B_{DC}}\cos(2\pi f_{AC} t). \tag{3}$$

We aim at $2\theta_0 \approx 90°$ by setting $|B_{AC0}/B_{DC}| = \tan\theta_0 \approx 1$.

The field $\boldsymbol{B}_{AC}(t)$ is generated by an electromagnet consisting of a high-permeability toroidal ferrite core with a gap of 0.7 cm

and roughly 150 Cu-wire turns. The magnet is driven by a power amplifier in constant-voltage mode. We found that for frequencies f_{AC} between 2 kHz and 10 kHz, the product $f_{AC}B_{AC0}$ was approximately constant, amounting to some 85kHz · mT. This observation indicates that the impedance of the magnet is dominated by its inductive reactance $\propto f_{AC}$. The field $\boldsymbol{B}_{DC}$ is generated by a permanent magnet placed at a variable distance from the sample. To minimize any mechanical and electromagnetic coupling of the AC magnetic field to adjacent optical components, the magnet system is vibration-isolated from the optical table.

For PM, we calibrate the amplitude and the phase of $\boldsymbol{B}_{AC}(t)$ at the sample position with respect to the driving voltage for all relevant modulation frequencies f_{AC} by a tesla meter (FM302, Projekt Elektronik Mess- und Regelungstechnik GmbH) and a Hall probe (AS-NTP-0,6). For DM, $\boldsymbol{B}_{AC}$ and $\boldsymbol{B}_{DC}$ are measured simultaneously with a three-axis Hall probe (AS-N3DM). The electromagnet does not significantly heat up during the measurements.

To monitor the magnetization state of the sample, we make use of the emitted THz wave and Eq. (1). In our first experiments, we additionally employ the magneto-optic (MO) Kerr effect (MOKE). To this end, the polarization rotation of a reflected continuous-wave laser beam (wavelength of 635 nm) is measured using an assembly of two nearly crossed polarizers, a photodiode, and an oscilloscope. The voltage signal due to the MOKE polarization rotation is given by $S_{MO} = \boldsymbol{a} \cdot \boldsymbol{M}$, where the vector $\boldsymbol{a}$ summarizes the magneto-optic coefficient of each magnetization component [33,34]. Because the incident MOKE laser beam is p-polarized, it follows that $a_x = 0$. As our samples exhibit an in-plane magnetic anisotropy and the external magnetic field has a negligible out-of-plane component, we have $M_z = 0$ and, thus,

$$S_{MO} = \boldsymbol{a} \cdot \boldsymbol{M} \propto M_y. \tag{4}$$

A. THz Waveforms and Spectra

We first characterize the STE output for opposite static external magnetic fields $\boldsymbol{B}_{ext} = \pm B_{DC}\boldsymbol{u}_x$, resulting in opposite static magnetizations $\boldsymbol{M} = \pm\boldsymbol{M}_0 = \pm M_{sat}\boldsymbol{u}_x$. Figure 2(a) shows typical THz signal waveforms $S_y(\tau, \boldsymbol{M})$ as a function of the delay τ between THz and gate pulse for $\boldsymbol{M} = \pm\boldsymbol{M}_0$. We observe that more than 99% of the peak signal reverses when the magnetization is reversed.

To test whether the signal reversal for $\boldsymbol{M} = \pm\boldsymbol{M}_0$ is uniform for all THz frequency components of the emitted waveform, we perform the measurement of Fig. 2(a) again, but measure the THz field with a 10 µm thick ZnTe (110) crystal in a dry air atmosphere, whose bandwidth extends from 1 to 40 THz [31,32]. Figure 2(b) shows the corresponding amplitude spectra $|\tilde{S}_y(\nu, \boldsymbol{M})|$ of THz signals $S_y(\tau, \boldsymbol{M})$ from the STE for $\boldsymbol{M} = \pm\boldsymbol{M}_0$, where $\tilde{S}_y(\nu, \boldsymbol{M})$ is the Fourier-transformed $S_y(\tau, \boldsymbol{M})$ at frequency ν. The two spectra are almost identical and cover the interval of about 1–30 THz.

The dip at approximately 5 THz [Fig. 2(b)] arises from the zero of the electro-optic coefficient of ZnTe at this frequency [31], while the feature at 10 THz originates from a two-phonon absorption process in the Ge wafer behind the STE [30]. The subsequent dips at approximately 13, 17, and 19 THz are related to the refractive-index features of the STE's sapphire substrate [35]. We account for this effect by calculating the STE impedance $\tilde{Z}(\nu)$, which connects the pump-induced sheet charge current density $\int \mathrm{d}z\, j_c(z)$ inside the STE stack [Fig. 1(a)] to the THz field directly behind the STE [14]. As seen in Fig. 2(b), the calculated $|\tilde{Z}(\nu)|$ of our STE reproduces the features well at 13, 17, and 19 THz.

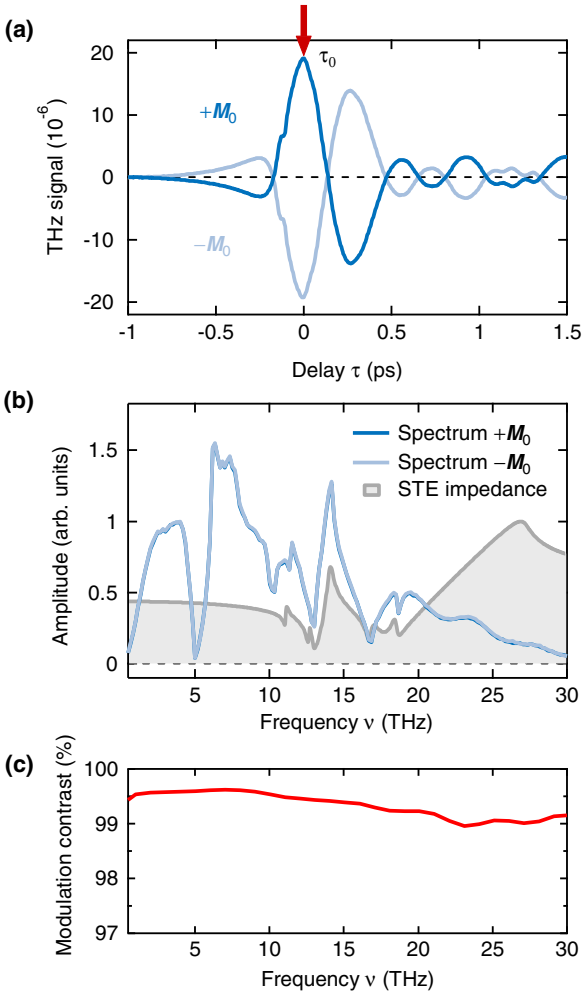

Fig. 2. Raw data and modulation contrast. (a) Typical THz signal waveforms $S_y(\tau, \boldsymbol{M})$ from the spintronic THz emitter for opposite magnetizations $\boldsymbol{M} = \pm\boldsymbol{M}_0$ measured with a 1 mm thick ZnTe (110) electro-optic crystal. For the modulation experiments, we measure the THz signal $S_j(t) = S_j(\tau_0, \boldsymbol{M}(t))$ (with $j = x$ or y) at the delay τ_0 of the maximum signal (red arrow) versus real time t. (b) Amplitude spectra $|\tilde{S}_y(\nu, \boldsymbol{M})|$ of THz signals $S_y(\tau, \boldsymbol{M})$ from the STE for $\boldsymbol{M} = \pm\boldsymbol{M}_0$ measured with a broadband 10 µm thick ZnTe (110) electro-optic crystal in dry air atmosphere. The gray curve shows the modulus $|\tilde{Z}(\nu)|$ of the calculated impedance of the STE including the sapphire substrate. (c) Modulation contrast of the STE versus frequency up to 30 THz.

Figure 2(c) shows the magnetization-related modulation contrast

$$C(\nu) = 1 - \frac{|1 + \tilde{R}(\nu)|}{1 + |\tilde{R}(\nu)|} \tag{5}$$

of the THz signal, where $\tilde{R}(\nu) = \tilde{S}_y(\nu, -\boldsymbol{M}_0)/\tilde{S}_y(\nu, +\boldsymbol{M}_0)$ is the complex-valued ratio of the Fourier-transformed THz signals obtained for $\boldsymbol{M} = \pm\boldsymbol{M}_0$, as shown in Fig. 2(b). Prior to the Fourier transformation, we apodize [36] the waveforms to minimize echoes caused by the 10 µm thick ZnTe detection crystal [31,32]. As seen in Fig. 2(b), C is larger than 99% throughout the range

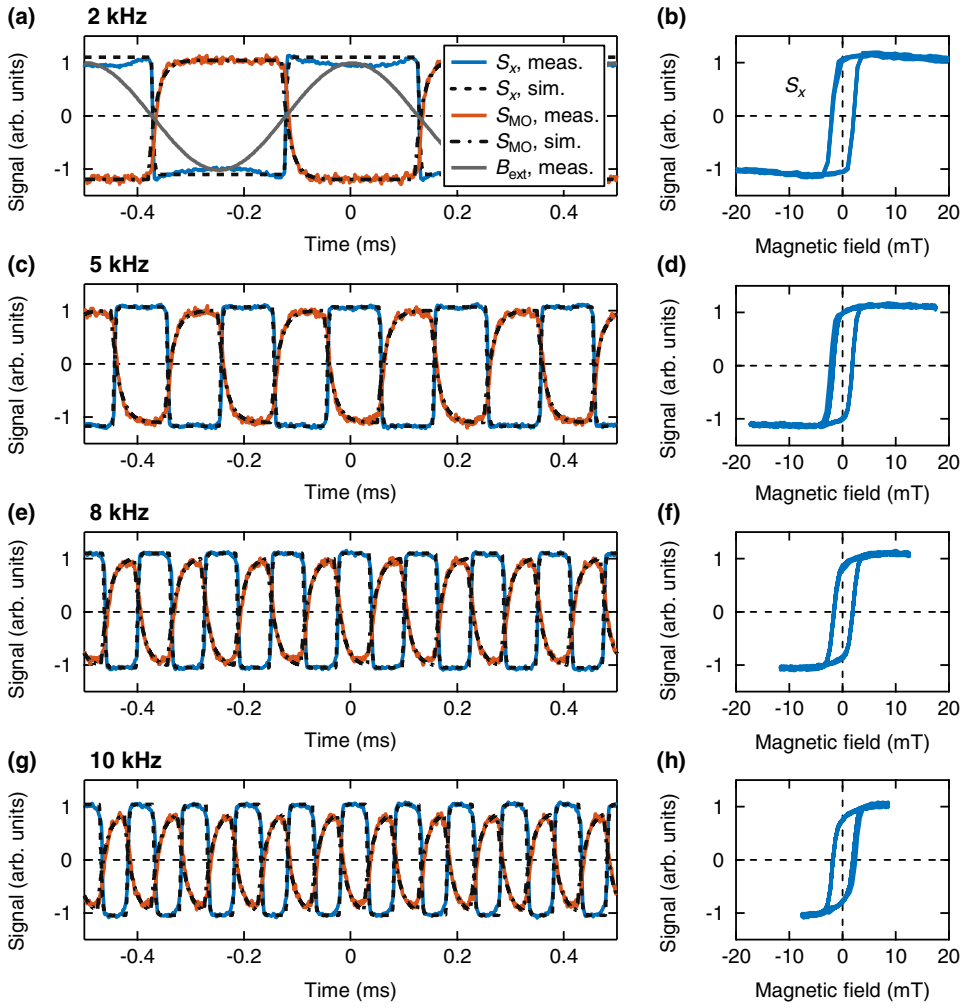

Fig. 3. Modulation of the THz-field polarity. (a) External magnetic field $B_{ext}(t)\boldsymbol{u}_x$, MOKE signal $S_{MO}(t) \propto M_y(t)$ and THz electro-optic signal $S_x(t) = S_x(\tau_0, \boldsymbol{M}(t)) \propto M_y(t)$ as a function of real time t for a modulation frequency of $f_{AC} = 2$ kHz of $B_{ext,y}$. Dashed lines are model calculations. The MOKE signal is inverted for clarity, and its DC component was removed. (b) THz signal amplitude $S_x(t)$ versus the external AC magnetic field $B_{ext,y}(t)$ for the data of the previous panel. (c–d) Same as panels (a–b), but for a modulation frequency f_{AC} of 5 kHz, (e–f) 8 kHz, and (g–h) 10 kHz, respectively.

1–30 THz [Fig. 2(b)]. We conclude that all THz frequency components emitted from the STE are modulated with a modulation contrast of more than 99%.

Note that this performance does not change as the magnetization becomes time-dependent, provided $\boldsymbol{M}(t)$ can still be considered static over the duration (<1 ps) [26] of the THz emission process. In other words, the STE operates quasistatically as long as the modulation frequency of $\boldsymbol{M}$ is significantly smaller than $1/1\text{ps} = 1$ THz. In the measurements shown here, this condition is safely fulfilled.

In the following experiments, we set $\tau = \tau_0$ at the maximum of the THz waveform [Fig. 2(a), red arrow], start modulating the sample magnetization $\boldsymbol{M} = \boldsymbol{M}(t)$, and subsequently record the signal $S_j(t) = S_j(\tau_0, \boldsymbol{M}(t))$ with $j = x$ or y as a function of real time t.

B. Polarity Modulation

In the PM mode [Fig. 1(b)], $\boldsymbol{B}_{ext}$ is parallel to the y axis and varies sinusoidally in time with frequency f_{AC}. Figure 3(a) (gray solid line) shows the measured $B_{ext,y}(t)$ over several cycles at a modulation frequency of 2 kHz. Because the coercive field of the STE is much smaller than the amplitude of $\boldsymbol{B}_{ext}$, we expect that the sample magnetization alternates between two opposite states $\pm M_{sat}\boldsymbol{u}_y$, as shown in Eq. (2).

Accordingly, the MOKE signal $S_{MO}(t)$ [red solid line in Fig. 3(a)] has a nearly square-like shape. The THz signal $S_x(t)$ [blue solid line in Fig. 3(a)] has dynamics similar to the MOKE signal $S_{MO}(t)$. This observation is consistent with the expected evolution of $\boldsymbol{M}(t)$ [Eq. (2)] and its impact on the signals $S_x(t)$ and $S_{MO}(t)$, as expected according to Eqs. (1) and (4).

We note, however, that $S_{MO}(t)$ and $S_x(t)$ of Fig. 3(a) exhibit two additional minor features that are not predicted by Eqs. (1) and (4): First, while the edges of the THz signal are steep, the MOKE signal appears to be smeared out over a time scale of about 100 µs. As shown below, this low-pass behavior arises from the photodiode circuitry. Second, the THz electro-optic signal is a superposition of a square-like waveform and a minor sinusoidal component at the same frequency f_{AC}, as shown in Fig. 3(a). The latter may arise from electromagnetic coupling of the circuitry generating $\boldsymbol{B}_{AC}$ and the electro-optic detection electronics or from mechanical coupling of $\boldsymbol{B}_{AC}$ to nearby optical components.

In Fig. 3(b), we display the THz signal amplitude $S_x(t) = S_x(\tau_0, \boldsymbol{M}(t))$ versus the external AC magnetic field $B_{ext,x}(t)$. We find a clear hysteresis loop. Its width implies a coercive field of

about 2 mT at 2 kHz, which is much smaller than $B_{AC0} = 42$ mT. Therefore, $\boldsymbol{M}$ nearly instantaneously follows $\boldsymbol{B}_{ext}$. The apparent decrease of the MOKE signal amplitude for increasing B_{AC0} can be traced back to the harmonic component mentioned above and discussed below.

Remarkably, we observe qualitatively identical dynamics when we increase the modulation frequency f_{AC} of the magnetic field to 5 kHz [Fig. 3(c)], 8 kHz [Fig. 3(e)], and to as high as 10 kHz [Fig. 3(g)], respectively. There are minor quantitative modifications: First, the low-pass characteristics of the MOKE signal becomes more pronounced as indicated by the decreased signal amplitude. Second, the sinusoidal component of the otherwise square-like THz signal decreases significantly when f_{AC} is increased from 2 kHz to 5 kHz. We ascribe this reduction to the reduced peak magnetic field, which has decreased from 42 mT to 17 mT, leading to a smaller electromagnetic or mechanical interference with the THz detection.

Note that the width of the hysteresis loop stays constant with increasing modulation frequency, as seen in Figs. 3(b), 3(d), 3(f), and 3(h). This observation indicates that the period $1/f_{AC}$ of the external magnetic field $\boldsymbol{B}_{ext}$ is long compared to the time it takes the magnetic moment of the probed STE volume to align parallel to the external magnetic field [37,38]. The approximately constant amplitude of all hysteresis loops shows that $\boldsymbol{B}_{ext}$ saturates the sample magnetization at all modulation frequencies up to 10 kHz.

1. Modeling of PM

To model the measured dynamics of Fig. 3, we calculate the magnetization using Eq. (2) and the external magnetic field $\boldsymbol{B}_{ext}(t) = \boldsymbol{B}_{AC}(t) = \boldsymbol{u}_y B_{AC0} \cos(2\pi f_{AC} t)$. Due to the nonvanishing coercive field $B_c \approx 2$mT of the STE, the switching of the STE magnetization is delayed by $\Delta t = B_c/2\pi f_{AC} B_{AC0}$ after $|\boldsymbol{B}_{AC}|$ has crossed zero. Because of $B_{AC0} f_{AC} \approx 85\text{kHz} \cdot \text{mT}$ (see above), we obtain $\Delta t \approx 4$ µs, which is taken into account in our model by a modified Eq. (2), $\boldsymbol{M}(t) = M_{sat} \boldsymbol{B}^0_{ext}(t - \Delta t)$.

The resulting MOKE and THz signals are obtained using the scaling relations of Eqs. (1) and (4). To account for the low-pass characteristics of the detection electronics, the calculated signals are convoluted with the respective filter impulse response functions $H(t) \propto \Theta(t) \exp(-t/\tau_{RC})$, where $\Theta(t)$ is the Heaviside step function. We estimate the time constant τ_{RC} by the product of the load resistance R and the capacitance C of the photodiode and connection cable. Based on the specifications of these components, we obtain $\tau_{RC} = RC \approx 50\,\text{k}\Omega \cdot 300\,\text{pF} = 15$ µs and $15\,\text{k}\Omega \cdot 100\,\text{pF} = 1.5$ µs for the MOKE and THz detection, respectively.

The only fit parameter is the global signal amplitude. As seen in Figs. 3(a), 3(c), 3(e), and 3(g), excellent agreement is obtained between measured (solid lines) and calculated (dashed lines) signals. We conclude that the polarity of THz pulses can be modulated by external magnetic fields at a rate of up to 10 kHz with a modulation contrast of more than 99%. Note that this contrast is only limited by a small nonmagnetic component of the emitted THz field of the STE, the origin and minimization of which might be the subject of future studies.

C. Direction Modulation

In the DM mode [Fig. 1(c)], we continuously and periodically rotate the sample magnetization between two angles $\pm\theta_0$ [see Eq. (3)]. To determine the relative size of M_x and M_y, we measure the THz signals S_y and S_x [see Eq. (1)]. Figure 4(a) schematically illustrates the situation.

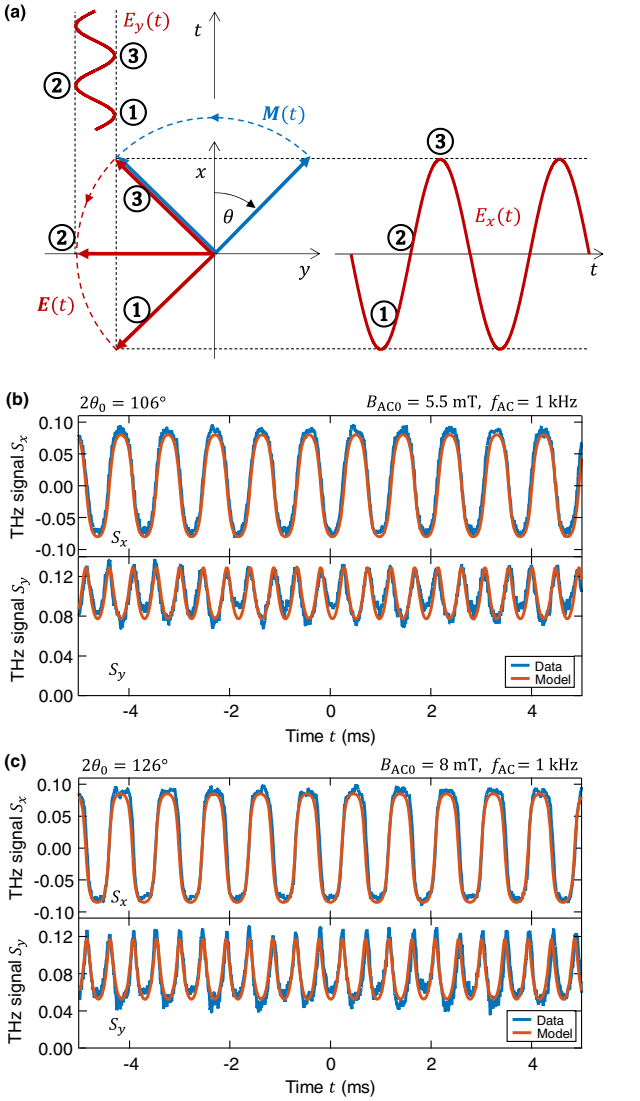

Fig. 4. Modulation of the THz polarization direction. (a) Schematic of expected THz signal amplitudes $S_x \propto E_x \propto -M_y$ and $S_y \propto E_y \propto M_x$ versus time, when the sample magnetization oscillates between angles $\pm\theta_0$. To determine the instantaneous angle θ, we measure the x and y amplitudes of the THz electric field. (b) Measured (blue) and modeled (orange) THz signal components S_x and S_y at a modulation frequency $f_{AC} = 1$ kHz and amplitude $B_{AC0} = 5.5$ mT. The amplitude ratio $|B_{AC0}/B_{DC}| = \tan\theta_0$ is such that $2\theta_0 = 106°$. (c) Same setting as in (b) but for $B_{AC0} = 8$ mT, yielding $2\theta_0 = 126°$.

The measured signal S_x at a DM frequency of $f_{AC} = 1$ kHz is shown in Fig. 4(b). It oscillates symmetrically around zero at the same frequency f_{AC} as the external magnetic field. For the signal S_y, we observe a markedly different behavior: It oscillates at twice the frequency $2f_{AC}$ of $\boldsymbol{B}_{AC}$, is located on top of a nonzero background, and has an asymmetric shape about its mean value. When we increase the amplitude of $\boldsymbol{B}_{AC}$ from 5.5 mT to 8 mT, the amplitude of S_x increases slightly, while the maxima of S_y remain constant and its minima decrease [Fig. 4(c)].

To understand the dynamics of S_x and S_y in detail, we consider the motion of the $\boldsymbol{M}$ vector [Fig. 4(a)]. It is fully described by the direction angle θ, which oscillates periodically between

$\pm\theta_0$ [Eq. (3)]. Figure 4(a) implies that the sign of the component $M_y \propto \sin\theta$ follows the sign of θ (see time labels ①, ③). It has, thus, the same periodicity and frequency as θ and is symmetric with respect to $\theta = 0$ (time label ②), consistent with our observations [Fig. 4(b)].

In contrast, the component $M_x \propto \cos\theta$ never changes sign and exhibits identical dynamics in the forward and backward motion of $\boldsymbol{M}$ [Fig. 4(a)]. Therefore, $M_x(t)$ has a significant nonzero offset, half the periodicity of $M_y(t)$ and, thus, oscillates at twice the frequency, $2f_{AC}$, in agreement with our measurements [Figs. 4(b), and 4(c)]. The asymmetry of $M_x(t)$ around its mean value arises because the maximum ($\theta = 0$; time label ②) is traversed with maximum magnetization rotation speed $\mathrm{d}\theta/\mathrm{d}t$ whereas the minima ($\theta = \pm\theta_0$; time labels ①, ③) coincide with the turning points of $\boldsymbol{M}$, at which $\mathrm{d}\theta/\mathrm{d}t$ vanishes. Finally, Fig. 4(a) indicates that θ_0 increases when B_{AC0} is increased, consistent with our observations (Fig. 4(b) versus Fig. 4(c)].

We note that S_x has a small DC component. It may, for instance, arise from a small component of $\boldsymbol{B}_{DC}$ along $\boldsymbol{B}_{AC}$ or from a small contribution of E_y to S_x because the THz polarizer may not be perfectly aligned.

1. Modeling of DM

To model the dynamics in the DM mode, we use a procedure similar to what was used for the PM mode, but account for the modified external field by $\boldsymbol{B}_{ext}(t) = \boldsymbol{B}_{AC}(t) + \boldsymbol{B}_{DC}$. Because all time constants of the THz detection electronics, including that of the lock-in amplifier (10 μs), are much smaller than the period $1/f_{AC} = 1$ ms, we do not consider them in the modeling.

Again, fitting our model to our data yields excellent agreement with the measured signals S_x and S_y, as shown by the dashed lines in Figs. 4(b), and 4(c). The fit procedure yields $2\theta_0 = 106°$ and 126° for the data of Fig. 4(b) and Fig. 4(c), respectively. These values are close to the target value of $2\theta_0 = 90°$. The minor deviation may arise from uncertainties in the calibration of the magnetic field: The sensors of the Hall probe are located at some depth below the surface of the device, which we approximately compensated for by shifting the probe. We conclude that we can also modulate the direction of the THz field polarization at kilohertz rates.

3. CONCLUSION

We have shown that the polarity of THz electromagnetic pulses from an STE can be controlled by external magnetic AC fields with a modulation contrast of better than 99% at modulation frequencies of up to 10 kHz. By adding a DC magnetic field, modulation of the direction of the THz peak field at kilohertz rates becomes possible. By tuning the strength of the external AC magnetic field, we demonstrated tailored rotation of the THz polarization plane. Our modulation approach is broadband and uniformly affects all spectral components of the THz pulse from 1 to 30 THz and beyond.

We anticipate that PM and, more generally, DM of the polarization of THz pulses both enable interesting applications in all kinds of modulation spectroscopy. For instance, PM is useful for low-noise lock-in detection of the THz signal. In contrast to a mechanical chopper, no moving parts are required, and the resulting signal is a factor of 2 larger. In nonlinear THz spectroscopy, one can easily separate effects that are symmetric (e.g., $\propto \boldsymbol{E}^2$) and antisymmetric (e.g., $\propto \boldsymbol{E}$) with respect to the driving THz field $\boldsymbol{E}$ [39].

DM is highly interesting for THz time-domain ellipsometry where the sample response to x- and y-polarized incident THz pulses is measured [40]. By fast modulation between x and y polarizations, we can quasi-simultaneously probe the optical properties of the sample along the x and y directions and, thus, strongly reduce the impact of possible setup drifts.

Rapid modulation of the sign and direction of the magnetization of a given sample is interesting for low-noise probing of small magnetic effects in materials by THz emission spectroscopy [20,26,41] and THz transmission spectroscopy [42].

We finally note that our approach can be extended to uniform rotation of the THz polarization plane and even higher modulation frequencies. Uniform rotation of the STE magnetization is achieved by superposition of two perpendicular harmonic magnetic fields with a phase difference of 90°. Regarding modulation speed, the hysteresis loops of Fig. 3 indicate that the switching time of the STE magnetization does not limit its modulation at frequencies up to 10 kHz. Therefore, modulation frequencies exceeding 100 kHz should be feasible.

Funding. Deutsche Forschungsgemeinschaft; European Union H2020 Program (681917); European Commission (863155).

Acknowledgment. The authors acknowledge funding by the German Research Foundation through the collaborative research center SFB TRR 227 "Ultrafast spin dynamics" (projects B02 and A05) and the European Union H2020 program through the project CoG TERAMAG/Grant No. 681917. The authors acknowledge financial support from the Horizon 2020 Framework Programme of the European Commission under FET-Open Grant No. 863155 (s-Nebula). The authors would like to thank Genaro Bierhance for fruitful discussions and the electronics workshop of Fritz Haber Institute of the Max Planck Society, in particular Viktor Platschkowski, Thomas Zehentbauer, and Georg Heyne, for their support in the development of the electromagnet.

Disclosures. Authors Oliver Gueckstock, Lukáš Nádvorník, Tom S. Seifert, Mathias Kläui, and Tobias Kampfrath have filed a patent application at the European Patent Office covering rapid polarization modulation of spintronic THz emitters.

Data availability. Data shown in the figures are available at [43]. Other data underlying the results presented in this paper may be obtained from the authors upon reasonable request.

REFERENCES

1. S. L. Dexheimer, *Terahertz Spectroscopy: Principles and Applications* (CRC Press, 2017).
2. S. S. Dhillon, M. S. Vitiello, E. H. Linfield, A. G. Davies, M. C. Hoffmann, J. Booske, C. Paoloni, M. Gensch, P. Weightman, G. P. Williams, E. Castro-Camus, D. R. S. Cumming, F. Simoens, I. Escorcia-Carranza, J. Grant, S. Lucyszyn, M. Kuwata-Gonokami, K. Konishi, M. Koch, C. A. Schmuttenmaer, T. L. Cocker, R. Huber, A. G. Markelz, Z. D. Taylor, V. P. Wallace, J. Axel Zeitler, J. Sibik, T. M. Korter, B. Ellison, S. Rea, P. Goldsmith, K. B. Cooper, R. Appleby, D. Pardo, P. G. Huggard, V. Krozer, H. Shams, M. Fice, C. Renaud, A. Seeds, A. Stöhr, M. Naftaly, N. Ridler, R. Clarke, J. E. Cunningham, and M. B. Johnston, "The 2017 terahertz science and technology roadmap," J. Phys. D **50**, 043001 (2017).
3. M. Rahm, J.-S. Li, and W. J. Padilla, "THz wave modulators: a brief review on different modulation techniques," J. Infrared, Millimeter, Terahertz Waves **34**, 1–27 (2012).
4. M. Tonouchi, "Cutting-edge terahertz technology," Nat. Photonics **1**, 97–105 (2007).
5. R. V. Morris, A. V. Stier, and N. P. Armitage, "Polarization modulation time-domain terahertz polarimetry," Opt. Express **20**, 12303–12317 (2012).
6. L. Wu, A. Farid, N. J. Laurita, T. Mueller, and N. P. Armitage, "A compact broadband terahertz range quarter-wave plate," J. Infrared, Millimeter, Terahertz Waves **41**, 642–654 (2020).

7. S. A. Baig, J. L. Boland, D. A. Damry, H. H. Tan, C. Jagadish, H. J. Joyce, and M. B. Johnston, "An ultrafast switchable terahertz polarization modulator based on III–V semiconductor nanowires," Nano Lett. **17**, 2603–2610 (2017).
8. M. Sato, T. Higuchi, N. Kanda, K. Konishi, K. Yoshioka, T. Suzuki, K. Misawa, and M. Kuwata-Gonokami, "Terahertz polarization pulse shaping with arbitrary field control," Nat. Photonics **7**, 724–731 (2013).
9. H. S. M. Beck, G. Klatt, J. Demsar, S. Winnerl, M. Helm, and T. Dekorsy, "Impulsive terahertz radiation with high electric fields from an amplifier-driven large-area photoconductive antenna," Opt. Express **18**, 9251–9257 (2010).
10. K. Maussang, J. Palomo, J. Mangeney, S. S. Dhillon, and J. Tignon, "Large-area photoconductive switches as emitters of terahertz pulses with fully electrically controlled linear polarization," Opt. Express **27**, 14784–14797 (2019).
11. Y. Hirota, R. Hattori, M. Tani, and M. Hangyo, "Polarization modulation of terahertz electromagnetic radiation by four-contact photoconductive antenna," Opt. Express **14**, 4486–4493 (2006).
12. N. Amer, W. C. Hurlbut, B. J. Norton, Y.-S. Lee, and T. B. Norris, "Generation of terahertz pulses with arbitrary elliptical polarization," Appl. Phys. Lett. **87**, 221111 (2005).
13. Q. Chen and X. C. Zhang, "Polarization modulation in optoelectronic generation and detection of terahertz beams," Appl. Phys. Lett. **74**, 3435–3437 (1999).
14. T. Seifert, S. Jaiswal, U. Martens, J. Hannegan, L. Braun, P. Maldonado, F. Freimuth, A. Kronenberg, J. Henrizi, I. Radu, E. Beaurepaire, Y. Mokrousov, P. M. Oppeneer, M. Jourdan, G. Jakob, D. Turchinovich, L. M. Hayden, M. Wolf, M. Münzenberg, M. Kläui, and T. Kampfrath, "Efficient metallic spintronic emitters of ultrabroadband terahertz radiation," Nat. Photonics **10**, 483–488 (2016).
15. T. Seifert, S. Jaiswal, M. Sajadi, G. Jakob, S. Winnerl, M. Wolf, M. Kläui, and T. Kampfrath, "Ultrabroadband single-cycle terahertz pulses with peak fields of 300 kV cm^{-1} from a metallic spintronic emitter," Appl. Phys. Lett. **110**, 252402 (2017).
16. D. Yang, J. Liang, C. Zhou, L. Sun, R. Zheng, S. Luo, Y. Wu, and J. Qi, "Powerful and tunable THz emitters based on the Fe/Pt magnetic heterostructure," Adv. Opt. Mater. **4**, 1944–1949 (2016).
17. D. M. Nenno, L. Scheuer, D. Sokoluk, S. Keller, G. Torosyan, A. Brodyanski, J. Losch, M. Battiato, M. Rahm, R. H. Binder, H. C. Schneider, R. Beigang, and E. T. Papaioannou, "Modification of spintronic terahertz emitter performance through defect engineering," Sci. Rep. **9**, 13348 (2019).
18. R. Schneider, M. Fix, J. Bensmann, S. Michaelis de Vasconcellos, M. Albrecht, and R. Bratschitsch, "Spintronic GdFe/Pt THz emitters," Appl. Phys. Lett. **115**, 152401 (2019).
19. Y. Wu, M. Elyasi, X. Qiu, M. Chen, Y. Liu, L. Ke, and H. Yang, "High-performance THz emitters based on ferromagnetic/nonmagnetic heterostructures," Adv. Mater. **29**, 1603031 (2017).
20. T. J. Huisman, R. V. Mikhaylovskiy, J. D. Costa, F. Freimuth, E. Paz, J. Ventura, P. P. Freitas, S. Blugel, Y. Mokrousov, T. Rasing, and A. V. Kimel, "Femtosecond control of electric currents in metallic ferromagnetic heterostructures," Nat. Nanotechnol. **11**, 455–458 (2016).
21. W. Wu, S. Lendinez, M. Taghipour Kaffash, R. D. Schaller, H. Wen, and M. B. Jungfleisch, "Modification of terahertz emission spectrum using microfabricated spintronic emitters," J. Appl. Phys. **128**, 103902 (2020).
22. J. Hawecker, T. H. Dang, E. Rongione, J. Boust, S. Collin, J.-M. George, H.-J. Drouhin, Y. Laplace, R. Grasset, J. Dong, J. Mangeney, J. Tignon, H. Jaffrès, L. Perfetti, and S. Dhillon, "Spin injection efficiency at metallic interfaces probed by THz emission spectroscopy," Adv. Opt. Mater., 2100412 (2021), Early View.
23. Z. Feng, H. Qiu, D. Wang, C. Zhang, S. Sun, B. Jin, and W. Tan, "Spintronic terahertz emitter," J. Appl. Phys. **129**, 010901 (2021).
24. T. S. Seifert, N. M. Tran, O. Gueckstock, S. M. Rouzegar, L. Nadvornik, S. Jaiswal, G. Jakob, V. V. Temnov, M. Münzenberg, M. Wolf, M. Kläui, and T. Kampfrath, "Terahertz spectroscopy for all-optical spintronic characterization of the spin-Hall-effect metals Pt, W and $Cu_{80}Ir_{20}$," J. Phys. D **51**, 364003 (2018).
25. T. Kampfrath, M. Battiato, P. Maldonado, G. Eilers, J. Notzold, S. Mahrlein, V. Zbarsky, F. Freimuth, Y. Mokrousov, S. Blugel, M. Wolf, I. Radu, P. M. Oppeneer, and M. Munzenberg, "Terahertz spin current pulses controlled by magnetic heterostructures," Nat. Nanotechnol. **8**, 256–260 (2013).
26. R. Rouzegar, L. Brandt, L. Nadvornik, D. A. Reiss, A. L. Chekhov, O. Gueckstock, C. In, M. Wolf, T. S. Seifert, P. W. Brouwer, G. Woltersdorf, and T. Kampfrath, "Laser-induced terahertz spin transport in magnetic nanostructures arises from the same force as ultrafast demagnetization," arXiv 2103.11710 (2021).
27. R. I. Herapath, S. M. Hornett, T. S. Seifert, G. Jakob, M. Kläui, J. Bertolotti, T. Kampfrath, and E. Hendry, "Impact of pump wavelength on terahertz emission of a cavity-enhanced spintronic trilayer," Appl. Phys. Lett. **114**, 041107 (2019).
28. E. T. Papaioannou, G. Torosyan, S. Keller, L. Scheuer, M. Battiato, V. K. Mag-Usara, J. L'huillier, M. Tani, and R. Beigang, "Efficient terahertz generation using Fe/Pt spintronic emitters pumped at different wavelengths," IEEE Trans. Magn. **54**, 9100205 (2018).
29. J. A. Fülöp, S. Tzortzakis, and T. Kampfrath, "Laser-driven strong-field terahertz sources," Adv. Opt. Mater. **8**, 1900681 (2019).
30. A. Singh, A. Pashkin, S. Winnerl, M. Helm, and H. Schneider, "Gapless broadband terahertz emission from a germanium photoconductive emitter," ACS Photon. **5**, 2718–2723 (2018).
31. A. Leitenstorfer, S. Hunsche, J. Shah, M. C. Nuss, and W. H. Knox, "Detectors and sources for ultrabroadband electro-optic sampling: experiment and theory," Appl. Phys. Lett. **74**, 1516–1518 (1999).
32. T. Kampfrath, J. Nötzold, and M. Wolf, "Sampling of broadband terahertz pulses with thick electro-optic crystals," Appl. Phys. Lett. **90**, 231113 (2007).
33. T. Kampfrath, R. G. Ulbrich, F. Leuenberger, M. Münzenberg, B. Sass, and W. Felsch, "Ultrafast magneto-optical response of iron thin films," Phys. Rev. B **65**, 104429 (2002).
34. C.-Y. You and S.-C. Shin, "Generalized analytic formulae for magneto-optical Kerr effects," J. Appl. Phys. **84**, 541–546 (1998).
35. A. S. Barker, "Infrared lattice vibrations and dielectric dispersion in corundum," Phys. Rev. **132**, 1474–1481 (1963).
36. D. A. Naylor and M. K. Tahic, "Apodizing functions for Fourier transform spectroscopy," J. Opt. Soc. Am. A **24**, 3644–3648 (2007).
37. D. C. Jiles, "Frequency dependence of hysteresis curves in conducting magnetic materials," J. Appl. Phys. **76**, 5849–5855 (1994).
38. G. B. V. Basso, A. Infortuna, and M. Pasquale, "Preisach model study of the connection between magnetic and microstructural properties of soft magnetic materials," IEEE Trans. Magn. **31**, 4000–4005 (1995).
39. M. Hudl, M. d'Aquino, M. Pancaldi, S. H. Yang, M. G. Samant, S. S. P. Parkin, H. A. Durr, C. Serpico, M. C. Hoffmann, and S. Bonetti, "Nonlinear magnetization dynamics driven by strong terahertz fields," Phys. Rev. Lett. **123**, 197204 (2019).
40. A. Rubano, L. Braun, M. Wolf, and T. Kampfrath, "Mid-infrared time-domain ellipsometry: application to Nb-doped $SrTiO_3$," Appl. Phys. Lett. **101**, 081103 (2012).
41. T. S. Seifert, S. Jaiswal, J. Barker, S. T. Weber, I. Razdolski, J. Cramer, O. Gueckstock, S. F. Maehrlein, L. Nadvornik, S. Watanabe, C. Ciccarelli, A. Melnikov, G. Jakob, M. Munzenberg, S. T. B. Goennenwein, G. Woltersdorf, B. Rethfeld, P. W. Brouwer, M. Wolf, M. Klaui, and T. Kampfrath, "Femtosecond formation dynamics of the spin Seebeck effect revealed by terahertz spectroscopy," Nat. Commun. **9**, 2899 (2018).
42. L. Nádvorník, M. Borchert, L. Brandt, R. Schlitz, K. A. de Mare, K. Výborný, I. Mertig, G. Jakob, M. Kläui, S. T. B. Goennenwein, M. Wolf, G. Woltersdorf, and T. Kampfrath, "Broadband terahertz probes of anisotropic magnetoresistance disentangle extrinsic and intrinsic contributions," Phys. Rev. X **11**, 021030 (2021).
43. O. Gueckstock, L. Nádvorník, T. S. Seifert, M. Borchert, G. Jakob, G. Schmidt, G. Woltersdorf, M. Kläui, M. Wolf, and T. Kampfrath, "Modulating the polarization of broadband terahertz pulses from a spintronic emitter at rates up to 10 kHz [Data set]," Zenodo (2021), https://zenodo.org/record/5017616.